GEOPHYSICS, VOL. 80, NO. 2 (MARCH-APRIL 2015); P. T91–T100, 10 FIGS., 2 TABLES.
10.1190/GEO2014-0420.1

Fast Huygens' sweeping methods for multiarrival Green's functions of Helmholtz equations in the high-frequency regime

Jianliang Qian[1], Songting Luo[2], and Robert Burridge[3]

ABSTRACT

Multiarrival Green's functions are essential in seismic modeling, migration, and inversion. Huygens-Kirchhoff (HK) integrals provide a bridge to integrate locally valid first-arrival Green's functions into a globally valid multiarrival Green's function. We have designed robust and accurate finite-difference methods to compute first-arrival traveltimes and amplitudes, so that first-arrival Green's functions can be constructed rapidly. We adapted a fast butterfly algorithm to evaluate discretized HK integrals. The resulting fast Huygens' sweeping method has the following unique features: (1) it precomputes a set of local traveltime and amplitude tables, (2) it automatically takes care of caustics, (3) it constructs Green's functions of the Helmholtz equation for arbitrary frequencies and for many point sources, and (4) for a fixed number of points per wavelength, it constructs each Green's function in nearly optimal complexity $O(N \log N)$ in terms of the total number of mesh points N, where the prefactor of the complexity only depends on the specified accuracy, and is independent of the frequency. The 2D and 3D examples revealed the performance of the method.

INTRODUCTION

Green's functions for the Helmholtz equation in inhomogeneous media are essential for seismic modeling, migration, and inversion. However, due to the highly oscillatory nature of wavefields, which induces the so-called dispersion (pollution) error (Babuska and Sauter, 2000), it is very costly and difficult for finite-difference or finite-element methods to directly solve the equation to high accuracy in the high-frequency regime; consequently, some approximate methods, such as the one-way wave equation and geometric-optics (GO)-based asymptotics are frequently appealed.

To construct Green's functions for the Helmholtz equation using GO, one popular approach is finite-differencing eikonal equations to compute first-arrival traveltimes (Vidale, 1990; van Trier and Symes, 1991; Qin et al., 1992; Schneider et al., 1992; Hole and Zelt, 1995; Schneider, 1995; Pica, 1997; Kim and Cook, 1999; Sethian and Popovici, 1999; Franklin and Harris, 2001; Qian and Symes, 2002a, 2002b; Tsai et al., 2003; Kao et al., 2004; Zhang et al., 2005, 2006; Zhao, 2005; Leung and Qian, 2006; Qian et al., 2007a, 2007b; Fomel et al., 2009; Alkhalifah and Fomel, 2010; Benamou et al., 2010; Serna and Qian, 2010; Luo and Qian, 2011, 2012; Luo et al., 2012). However, in Geoltrain and Brac (1993) and Gray and May (1994), prestack Kirchhoff depth migration using first-arrival Green's functions are questioned in imaging complex structures that host multiple transmitted arrivals because the first-arrival traveltimes in complex media usually do not correspond to the most energetic traveltimes crucial for imaging complex structures (Nichols, 1994); furthermore, Geoltrain and Brac (1993) suggest using dynamically correct multiarrival Green's functions, in which multivalued eikonals and amplitudes are correctly accounted for. Consequently, Operto et al. (2000) extend the asymptotic ray-Born migration/inversion originally designed to process one single arrival to the case of multiple arrivals using ray theory-based dynamically correct multiarrival Green's functions, so as to account for the cross contributions of all the source-receiver raypaths; naturally, it is nontrivial to construct such ray-theory Green's functions because they have to explicitly keep track of caustics, ray branches, and the Keller-Maslov index, so that multivalued phases and amplitudes are correctly taken into consideration (Červený et al., 1977; Chapman, 1985). As an alternative, Gaussian beams are able to take care of multiple arrivals and caustics automatically in ray theory asymptotics for Green's functions at the cost of expensive beam summations (Červený et al., 1982; Popov, 1982; Ralston, 1983; Hill, 1990; Albertin et al., 2004; Gray, 2005; Leung

Manuscript received by the Editor 3 September 2014; revised manuscript received 19 November 2014; published online 27 February 2015.
[1]Michigan State University, Department of Mathematics, East Lansing, Michigan, USA. E-mail: qian@math.msu.edu.
[2]Iowa State University, Department of Mathematics, Ames, Iowa, USA. E-mail: luos@iastate.edu.
[3]University of New Mexico, Department of Mathematics and Statistics, Albuquerque, New Mexico, USA. E-mail: burridge137@gmail.com.

et al., 2007; Tanushev et al., 2007; Hu and Stoffa, 2009; Leung and Qian, 2010; Qian and Ying, 2010a, 2010b; Bao et al., 2014).

On the other hand, Bevc (1997) proposes a semirecursive Kirchhoff depth migration method to image complex structures by combining wave equation datuming (Berryhill, 1979) and first arrival-based Kirchhoff migration (Geoltrain and Brac, 1993). Bevc (1997) succeeds in obtaining accurate images of complex structures by breaking up the structure into small depth regions, so that traveltime fields emanated from point sources located in the small depth regions do not develop the adverse effects of caustics, head waves, and multiple arrivals; correspondingly, first-arrival Green's functions are physically correct in each small depth region, so that first-arrival Kirchhoff migrations are accurate in imaging the corresponding small depth region, where Berryhill's (1979) wave equation datuming technique is used to prepare the data for the Kirchhoff migration in each small depth region (see Li and Fomel [2013] for a recent implementation of this migration method). In fact, Bevc's (1997) approach amounts to constructing a kinematically correct multiarrival Green's function implicitly and indirectly using first arrivals of Huygens' secondary sources. Given that first arrivals are easy to compute by finite-differencing eikonal equations, a natural question is, can we construct dynamically correct multiarrival Green's functions explicitly using first arrivals and related amplitudes of Huygens' secondary sources? Such multiarrival Green's functions will find wide applications not only in prestack Kirchhoff depth migrations but also in wave equation-based migrations. Recently, Luo et al., 2014a propose a Eulerian GO method, the fast Huygens' sweeping method, for constructing exactly such multiarrival Green's functions by finite-differencing eikonal and transport equations corresponding to Huygens' secondary sources and integrating physically valid, first-arrival Green's functions of secondary sources with the Huygens-Kirchhoff (HK) integral formula (Burridge, 1962; Baker and Copson, 1987).

The idea of the fast Huygens' sweeping method (Luo et al., 2014a) can be summarized as follows: In some applications, it is reasonable to assume that geodesics (rays) have a consistent orientation, so that the Helmholtz equation may be viewed as an evolution equation in one of the spatial directions. With such applications in mind, the fast Huygens' sweeping method can be used for computing Green's functions of Helmholtz equations in inhomogeneous media in the high-frequency regime and in the presence of caustics. The first novelty of the method is that the HK secondary source principle is used to integrate many locally valid asymptotic solutions to yield a globally valid asymptotic solution, so that caustics associated with the usual GO ansatz can be treated automatically. The second novelty is that a butterfly algorithm is adapted to carry out the matrix-vector products induced by the HK integration in $O(N \log N)$ operations, where N is the total number of mesh points, and the proportionality constant depends on the desired accuracy and is independent of the frequency parameter. To reduce the storage of the resulting traveltime and amplitude tables, each table is compressed into a linear combination of tensor-product-based multivariate Chebyshev polynomials, so that the information of each table is encoded into a small number of Chebyshev coefficients. As a result, the method enjoys the following desired features: (1) it precomputes a set of local traveltime and amplitude tables, (2) it automatically takes care of caustics, (3) it constructs Green's functions of the Helmholtz equation for arbitrary frequencies and for many point sources, and (4) for a fixed number of points per wavelength, it constructs each Green's function in nearly optimal complexity in terms of the total number of mesh points, where the prefactor of the complexity only depends on the specified accuracy and is independent of the frequency parameter.

In this work, we further develop the fast Huygens' sweeping method by designing more efficient and robust finite-difference methods for computing first-arrival traveltimes and corresponding amplitudes, and we carry out systematic comparisons between our globally valid asymptotic Green's functions and those obtained by directly finite differencing Helmholtz equations for various models, including the Marmousi model.

Our fast Huygens' sweeping method allows vertical and lateral variations in velocity fields as long as the velocity fields host rays with a consistent orientation, such as downgoing or upgoing, and the resulting wavefield has no aperture limitation, which is different from that obtained by solving an aperture-limited one-way wave equation. In the context of fully recursive *f-x* migration as illustrated in Gray and May (1994), our method can be viewed as a semirecursive *f-x* modeling method, so that it is natural to further develop the methodology into a semirecursive *f-x* migration method, and this is an ongoing project.

The paper is organized as follows: We start to present the factorization approaches and Babich's (1965) formulation for computing phases and amplitudes, so as to construct locally valid GO Green's functions. High-order factorizations and approximations of phases and amplitudes near source points will be presented. Then, we recall the fast Huygens' sweeping method for constructing globally valid asymptotic Green's functions. The 2D and 3D numerical experiments are presented to demonstrate the performance of our methods. Concluding remarks are given at the end.

HIGH-ORDER APPROXIMATION OF EIKONAL AND AMPLITUDE

We consider the Helmholtz equation with a point-source condition in the high-frequency regime:

$$\nabla_{\mathbf{r}}^2 U + \frac{\omega^2}{v^2(\mathbf{r})} U = -\delta(\mathbf{r} - \mathbf{r}_0), \tag{1}$$

with the Sommerfeld radiation condition imposed at infinity, where $U(\mathbf{r}, \omega; \mathbf{r}_0)$ is the wavefield, ω is the frequency, $v(\mathbf{r})$ is the wave speed, $\mathbf{r}_0 \equiv (x_0, y_0, z_0)$ is the source point, and $\nabla_{\mathbf{r}}^2$ denotes the Laplacian at $\mathbf{r} \equiv (x, y, z)$. The GO large-$\omega$ ansatz for Green's function with respect to a generic source $\mathbf{r}'$

$$G(\mathbf{r}, \omega; \mathbf{r}') \approx A(\mathbf{r}; \mathbf{r}') e^{i\omega\tau(\mathbf{r};\mathbf{r}')} \text{ in 3D}, \quad \left(\approx \frac{1}{\sqrt{\omega}} A(\mathbf{r}; \mathbf{r}') e^{i(\omega\tau(\mathbf{r};\mathbf{r}')+\pi/4)} \text{in 2D} \right) \tag{2}$$

yields the eikonal equation for phase τ and the transport equation for amplitude A, respectively,

$$|\nabla_{\mathbf{r}} \tau| = \frac{1}{v(\mathbf{r})}, \quad \tau(\mathbf{r}'; \mathbf{r}') = 0, \tag{3}$$

$$\nabla_{\mathbf{r}} \cdot (A^2 \nabla_{\mathbf{r}} \tau) = 0, \quad A(\mathbf{r}'; \mathbf{r}') = A'(\mathbf{r}'). \tag{4}$$

Because τ and A are locally smooth in a neighborhood of the source $\mathbf{r}'$ excluding the source itself (Milnor, 1963; Symes and Qian, 2003), they yield a valid GO Green's function in that local neighborhood. Here, τ and A are weakly coupled in the sense that τ must be computed first by solving eikonal equation 3 and then substituted in transport equation 4 for computing A. Because the Laplacian of τ is involved in equation 4, to get lth order accurate A, at least $(l+2)$th order accurate τ is required. Due to the source singularity because τ behaves like a distance function, which is nondifferentiable at the source point (Qian and Symes, 2002a), computing high-order accurate τ and A by finite-differencing equations 3 and 4 is not a trivial matter. Without special treatments of source singularities, any high-order finite-difference methods for solving equations 3 and 4 can formally have at most first-order accuracy and large errors.

High-order factorization for eikonals

We first recall a factorization approach to resolving the source singularity for computing τ (Pica, 1997; Zhang et al., 2005; Fomel et al., 2009; Luo and Qian, 2011, 2012; Luo et al., 2012). In the factorization approach, τ is factored as

$$\tau = \tilde{\tau}\,\bar{\tau}, \tag{5}$$

where $\tilde{\tau}$ is predetermined analytically to capture the source singularity, such that $\bar{\tau}$ is the new unknown that is smooth at the source and satisfies the factored eikonal equation:

$$|\tilde{\tau}\nabla_{\mathbf{r}}\bar{\tau} + \bar{\tau}\nabla_{\mathbf{r}}\tilde{\tau}| = 1/v(\mathbf{r}). \tag{6}$$

For instance, $\tilde{\tau}$ may be taken as $\tilde{\tau}(\mathbf{r};\mathbf{r}') = |\mathbf{r}-\mathbf{r}'|/v(\mathbf{r}')$.

Because $\bar{\tau}$ is smooth at the source, we can solve equation 6 efficiently with high-order Lax-Friedrichs weighted essentially nonoscillatory (LxF-WENO) schemes as designed in Kao et al. (2004), Zhang et al. (2006), Luo and Qian (2011), and Luo et al. (2012). In a Pth order, LxF-WENO finite-difference method on a mesh of size h, $\bar{\tau}$ must be initialized in the neighborhood of size $2(P-1)h$ centered at the source, and these initial values are fixed during iterations. Luo et al. (2014b) introduce an accurate, efficient, and systematic approach to initialize $\bar{\tau}$ near the source. Based on the power series expansion of τ^2, which is smooth near the source, one can derive approximations of τ near the source up to an arbitrary order of accuracy.

We recall the derivation of the high-order approximation of τ near the source. Assume that $T(\mathbf{r}) \equiv \tau^2(\mathbf{r})$ and $S(\mathbf{r}) \equiv 1/v^2(\mathbf{r})$ are analytic at the source, which is set to be the origin without loss of generality. We can expand T and S as a power series:

$$T(\mathbf{r}) = \sum_{\nu=0}^{\infty} T_\nu(\mathbf{r}), \quad S(\mathbf{r}) = \sum_{\nu=0}^{\infty} S_\nu(\mathbf{r}), \tag{7}$$

where T_ν and S_ν are homogeneous polynomials of degree ν in $\mathbf{r}$. From the eikonal equation 3, we have

$$\mathrm{ST} = \frac{1}{4}|\nabla_{\mathbf{r}}T|^2. \tag{8}$$

By substituting equation 7 into equation 8, we have

$$\left(\sum_{\nu=0}^{\infty} S_\nu(\mathbf{r})\right)\left(\sum_{\nu=0}^{\infty} T_\nu(\mathbf{r})\right) = \frac{1}{4}\left(\sum_{\nu=0}^{\infty} \nabla_{\mathbf{r}}T_\nu(\mathbf{r})\right)^2, \tag{9}$$

from which one can derive $\{T_\nu\}$ term by term by collecting terms of the same degree. Following Luo et al. (2014b), we can derive $T_0(\mathbf{r}) = 0, T_1(\mathbf{r}) = 0, T_2(\mathbf{r}) = S_0\mathbf{r}^2$, and a recursive formula for computing $T_P(\mathbf{r})$ for $P \geq 3$:

$$\begin{aligned}&(P-1)\,S_0\,T_P(\mathbf{r})\\ &= \sum_{\nu=1}^{P-2} S_\nu(\mathbf{r})\,T_{P-\nu}(\mathbf{r}) - \frac{1}{4}\sum_{\nu=2}^{P-2}\nabla_{\mathbf{r}}T_{\nu+1}(\mathbf{r})\cdot\nabla_{\mathbf{r}}T_{P-\nu+1}(\mathbf{r}).\end{aligned} \tag{10}$$

Then, we use the truncated sum $\tilde{T}_P \equiv \sum_{\nu=2}^{P} T_\nu$ to approximate T near the source, and we further choose $\tilde{\tau}_P \equiv \sqrt{\tilde{T}_P}$ to approximate τ near the source with accuracy of $|\tau(\mathbf{r}) - \tilde{\tau}_P(\mathbf{r})| = O(|\mathbf{r}|^P)$, $|\mathbf{r}| \to 0$.

Taking $\tilde{\tau}_P$ as high-order approximations of τ near the source, we apply high-order LxF-WENO methods to solve the factored equation 6. In the Pth order LxF-WENO method for solving equation 6 to obtain $\bar{\tau}$, we first choose $\tilde{\tau}(\mathbf{r}) \equiv \sqrt{S_0}|\mathbf{r}|$. To initialize $\bar{\tau}$ near the source, $\bar{\tau}$ is assigned as one at the source and as $\tilde{\tau}_P/\tilde{\tau}$ at other points in the $2(P-1)h$ neighborhood of the source, so that these values are fixed during the LxF-WENO sweeping iterations. At other points, the LxF-WENO iterations are used to update $\bar{\tau}$ with $\tilde{\tau}(\mathbf{r}) \equiv \sqrt{S_0}|\mathbf{r}|$.

High-order factorization for amplitudes

We extend the above factorization approach to deal with the amplitude A near the source. Because A is singular at the source, we introduce Babich's (1965) formulation,

$$B = A\tau^{(d-1)/2}, \tag{11}$$

into transport equation 4 for A, so that we have Babich's (1965) transport equation for the amplitude factor B:

$$\nabla_{\mathbf{r}}T(\mathbf{r})\cdot\nabla_{\mathbf{r}}B(\mathbf{r}) + B(\mathbf{r})\left[\frac{1}{2}\nabla_{\mathbf{r}}^2T(\mathbf{r}) - d/v^2(\mathbf{r})\right] = 0, \tag{12}$$

where d is the spatial dimension and $T(\mathbf{r}) = \tau^2(\mathbf{r})$. Because the amplitude factor B is smooth near and at the source (Babich, 1965) whereas the original amplitude A is singular at the source, we will use this transport equation to derive high-order approximations of B near the source. In addition, to power series expansions in equation 7, we assume that B's power series expansion is given as

$$B(\mathbf{r}) = \sum_{\nu=0}^{\infty} B_\nu(\mathbf{r}), \tag{13}$$

where B_ν are homogeneous polynomials of degree ν in $\mathbf{r}$. It follows that B_ν can be determined term by term by substituting equation 13 into equation 12:

$$\left(\sum_{\nu=2}^{\infty}\nabla_{\mathbf{r}}T_{\nu}(\mathbf{r})\right)\cdot\left(\sum_{\nu=1}^{\infty}\nabla_{\mathbf{r}}B_{\nu}(\mathbf{r})\right)+\left(\sum_{\nu=0}^{\infty}B_{\nu}(\mathbf{r})\right)\left[\frac{1}{2}\left(\sum_{\nu=2}^{\infty}\nabla_{\mathbf{r}}^{2}T_{\nu}(\mathbf{r})\right)-d\left(\sum_{\nu=0}^{\infty}S_{\nu}(\mathbf{r})\right)\right]=0. \tag{14}$$

We know from Babich (1965) that $B_0=1/2\sqrt{2\pi}$, for $d=2$, and $B_0=\sqrt{S_0}/4\pi$, for $d=3$.

Comparing the linear terms in equation 14 and using the homogeneity of B_1, we have

$$\begin{aligned}&\nabla_{\mathbf{r}}T_2\cdot\nabla_{\mathbf{r}}B_1+\frac{1}{2}(B_0\nabla_{\mathbf{r}}^2T_3+B_1\nabla_{\mathbf{r}}^2T_2)-d(B_0S_1+B_1S_0)\\&=0,\\&\Rightarrow 2S_0\mathbf{r}\cdot\nabla_{\mathbf{r}}B_1+\frac{1}{2}(B_0\nabla_{\mathbf{r}}^2T_3+2B_1dS_0)-d(B_0S_1+B_1S_0)\\&=0,\\&\Rightarrow 2S_0B_1+\frac{1}{2}B_0\nabla_{\mathbf{r}}^2T_3-dB_0S_1=0,\\&\Rightarrow B_1=\frac{1}{2S_0}(-\frac{1}{2}B_0\nabla_{\mathbf{r}}^2T_3+dB_0S_1).\end{aligned} \tag{15}$$

Equating Pth-degree terms on both sides of equation 14, we have

$$B_P=\frac{1}{2PS_0}\left(-\sum_{\nu=1}^{P-1}\nabla_{\mathbf{r}}B_{\nu}(\mathbf{r})\cdot\nabla_{\mathbf{r}}T_{P+2-\nu}(\mathbf{r})-\frac{1}{2}\sum_{\nu=0}^{P-1}B_{\nu}(\mathbf{r})\nabla_{\mathbf{r}}^2T_{P+2-\nu}(\mathbf{r})+d\sum_{\nu=0}^{P-1}B_{\nu}(\mathbf{r})S_{P-\nu}(\mathbf{r})\right). \tag{16}$$

Consequently, we can now use the truncated sum to approximate B; i.e.,

$$\tilde{B}_P\equiv\sum_{\nu=0}^{P}B_{\nu}, \tag{17}$$

and $|\tilde{B}_P-B|=O(|\mathbf{r}|^P),|\mathbf{r}|\to 0$.

Taking $\tilde{B}_P$ as a high-order approximation of B near the source, we will apply high-order LxF-WENO methods to solve Babich's (1965) transport equation 12 for B. In the Pth-order LxF-WENO method for solving equation 12, B is assigned as $\tilde{B}_P$ in the $2(P-1)h$-neighborhood of the source, so that these values are fixed during the LxF-WENO iterations; at other points, the LxF-WENO iterations are used to update B.

Comparing with the adaptive mesh refinement method for treating the source singularity used in Kim and Cook (1999) and Qian and Symes (2002a), high-order factorization-based LxF-WENO sweeping methods make computing high-order accurate $\bar{\tau}$ and B easy and efficient, resulting in high-order accurate τ and A and locally valid first-arrival Green's functions. If one is satisfied with accurate first-arrival Green's functions, then the schemes developed above suffice. However, because in general one needs multiarrival Green's functions, we incorporate these first-arrival Green's functions into the fast Huygens' sweeping method introduced in Luo et al. (2014a) to build globally valid multiarrival Green's functions.

HUYGENS'-PRINCIPLE-BASED GLOBALLY VALID GREEN'S FUNCTIONS

Assume that a domain Ω is illuminated by an exterior source $\mathbf{r}_0\notin\Omega$, and $\mathcal{S}=\partial\Omega$ is the closed surface enclosing the domain Ω (see Figure 1a). At any observation point $\mathbf{r}\in\Omega$, the wavefield $U(\mathbf{r};\mathbf{r}_0)$ excited by the source $\mathbf{r}_0$ can be written as the HK integral over $\mathcal{S}$ (Burridge, 1962; Baker and Copson, 1987):

$$\begin{aligned}U(\mathbf{r};\mathbf{r}_0)&=\int_{\mathcal{S}}\{G(\mathbf{r}';\mathbf{r})\nabla_{\mathbf{r}'}U(\mathbf{r}';\mathbf{r}_0)\\&\quad\cdot\mathbf{n}(\mathbf{r}')-U(\mathbf{r}';\mathbf{r}_0)\nabla_{\mathbf{r}'}G(\mathbf{r}';\mathbf{r})\cdot\mathbf{n}(\mathbf{r}')\}\mathrm{d}S(\mathbf{r}')\\&=\int_{\mathcal{S}}\{G(\mathbf{r};\mathbf{r}')\nabla_{\mathbf{r}'}U(\mathbf{r}';\mathbf{r}_0)\\&\quad\cdot\mathbf{n}(\mathbf{r}')-U(\mathbf{r}';\mathbf{r}_0)\nabla_{\mathbf{r}'}G(\mathbf{r};\mathbf{r}')\cdot\mathbf{n}(\mathbf{r}')\}\mathrm{d}S(\mathbf{r}'),\end{aligned} \tag{18}$$

where $G(\mathbf{r};\mathbf{r}')=G(\mathbf{r}';\mathbf{r})$ by reciprocity, $\mathbf{n}(\mathbf{r}')$ is the outward normal to $\mathcal{S}$ at $\mathbf{r}'=(x',y',z')$, and $G(\mathbf{r};\mathbf{r}')$ is the Green's function associated with the source $\mathbf{r}'$. In the integral, $G(\mathbf{r};\mathbf{r}')$ and $\nabla_{\mathbf{r}'}G(\mathbf{r};\mathbf{r}')\cdot\mathbf{n}(\mathbf{r}')$ associated with $\mathbf{r}'$ on $\mathcal{S}$ can be approximated with the GO ansatz 2.

By retaining the leading-order term after substituting equation 2 into equation 18, we have

$$\begin{aligned}U(\mathbf{r};\mathbf{r}_0)&\approx\int_{\mathcal{S}}\{G(\mathbf{r};\mathbf{r}')[\nabla_{\mathbf{r}'}U(\mathbf{r}';\mathbf{r}_0)\cdot\mathbf{n}(\mathbf{r}')]-G(\mathbf{r};\mathbf{r}')\nabla_{\mathbf{r}'}\tau(\mathbf{r};\mathbf{r}')\\&\quad\cdot\mathbf{n}(\mathbf{r}')[i\omega U(\mathbf{r}';\mathbf{r}_0)]\}\mathrm{d}S(\mathbf{r}')\\&\approx\int_{\mathcal{S}}\{G(\mathbf{r};\mathbf{r}')[\nabla_{\mathbf{r}'}U(\mathbf{r}';\mathbf{r}_0)\cdot\mathbf{n}(\mathbf{r}')]\\&\quad-G(\mathbf{r};\mathbf{r}')\cos(\theta(\mathbf{r};\mathbf{r}'))[i\omega U(\mathbf{r}';\mathbf{r}_0)/v(\mathbf{r}')]\}\mathrm{d}S(\mathbf{r}'),\end{aligned} \tag{19}$$

where θ is the takeoff angle of the ray from source $\mathbf{r}'$ to receiver $\mathbf{r}$ and is constant along the ray; i.e.,

$$\nabla_{\mathbf{r}}\theta(\mathbf{r};\mathbf{r}')\cdot\nabla_{\mathbf{r}}\tau(\mathbf{r};\mathbf{r}')=0, \tag{20}$$

consequently,

$$\nabla_{\mathbf{r}}\cos(\theta(\mathbf{r};\mathbf{r}'))\cdot\nabla_{\mathbf{r}}\tau(\mathbf{r};\mathbf{r}')=0. \tag{21}$$

Because the first-arrival GO approximations of Green's functions associated with the secondary sources are valid only locally, equation 19 can only be used in a narrow band near $\mathcal{S}$, so that rays emanating from the source have not yet developed caustics. Hence, the fast Huygens' sweeping method carries out integration 19 in a layer-by-layer manner (see Figures 1b and 2). The secondary sources are placed on the top boundary of each layer, and HK integral 19 is performed inside each layer.

Layer-based Huygens' sweeping

We recall the planar-layer-based Huygens' sweeping method (Luo et al., 2014a) as illustrated in Figures 1b and 2 and summarized below.

Algorithm: Algorithmic sketch for Huygens' sweeping method

- Stage 1 (offline): Precompute asymptotic ingredients, such as phases, amplitudes, and takeoff angles. Because these ingredients only depend on the velocity and do not depend on wavelength or frequency, they can be computed on very coarse meshes using high-order schemes. We carry out the following steps: (1) the whole computational domain is partitioned into layers as in Figure 1b, so that rays emanating from the primary source and each secondary source have not yet developed caustics, (2) the tables of phases, amplitudes, and takeoff angles with respect to the primary source in the first layer (see Figure 2a) as well as those tables for each secondary source located on the layer boundary of the other layers (see Figure 2b) are computed by solving the relevant equations as described above with high-order LxF-WENO methods in the corresponding layer, and (3) these tables are compressed with the Chebyshev expansion-based data compression technique (Boyd, 2001; Alkhalifah, 2011; Luo et al., 2014a; see Appendix A).
- Stage 2 (online): Given a frequency ω, we specify 4–6 points per wavelength, so that the wavefield is sampled with n mesh points along each dimension: (1) in the first layer containing the primary source, construct the first-arrival Green's function with tables of the primary source (see Figure 2a), (2) from the second layer to all the other layers, for each line of secondary sources on the layer boundary, tables of phases, amplitudes, and takeoff angles are read from the hard drive, and they are used to reconstruct the tables on the underlying mesh by Chebyshev sums (see Appendix A); if necessary, the tables are interpolated with respect to the secondary sources onto the underlying mesh, and (3) HK integral 19 is then discretized with a numerical quadrature rule, such as the trapezoidal rule as used in the current work, and the resulting matrix-vector products are evaluated by a fast butterfly algorithm as shown in Luo et al. (2014a) (see Figure 2b).

Complexity analysis

In the above algorithm, two sets of different meshes are involved in the computation. One set of meshes is used for computing GO ingredients; because these ingredients are independent of wavelength or frequency, these meshes are independent of wavelength as well and can be very coarse, so that high-order schemes still can yield sufficiently accurate GO ingredients. The other set of meshes is used to sample the wavefield. Because we need to specify four to six points per wavelength to resolve wave oscillations, these meshes depend on the wavelength or frequency. Therefore, the following complexity analysis treats the two sets of meshes differently.

Assume that there are L layers in the partition. In stage 1, the complexity of computing each table in each layer with LxF-WENO methods is $O(m^{d-1}(m/L)\log m)$, where m mesh points are used for each spatial direction and the log m factor comes from the number of sweeping iterations. Because there are $O(m^{d-1})$ secondary sources for each layer, the total complexity of computing all the tables for secondary sources is $\mathrm{LO}(m^{d-1}(m^{d-1}(m/L)\log m)) = O(m^{2d-1}\log m)$, which is analogous to the computational

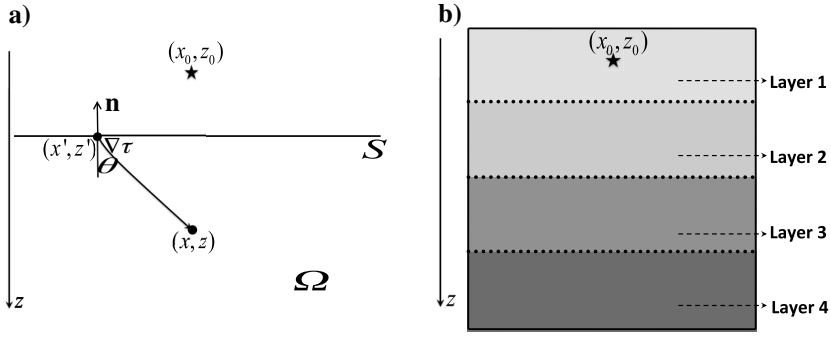

Figure 1. The 2D demonstration of the HK integral and partition of the domain into layers: (a) HK integral with S an infinite plane and (b) partition of the domain into planar layers. The star represents the primary source.

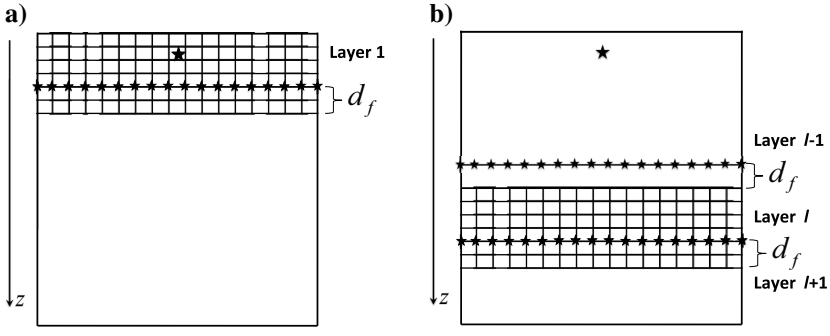

Figure 2. Receivers and sources in the HK integral and illustration of the fast Huygens' sweeping algorithm. The larger star represents the primary source, little stars represent the secondary sources on the boundary of each layer, and the grid represents the mesh. In offline stage 1, the coarse mesh is used. In online stage 2, the refined mesh is used and depends on ω. The region of size d_f is independent of ω. Panel (a) shows the first layer with respect to the primary source and panel (b) shows a layer l with $l > 1$ and with respect to secondary sources on the boundary of this layer.

complexity for asymptotic ingredients in the phase space (Symes and Qian, 2003; Leung et al., 2007; Luo et al., 2014a). Because these tables are precomputed and are independent of wavelength or frequency, they can be computed on very coarse meshes using high-order schemes and can be reused for different frequencies.

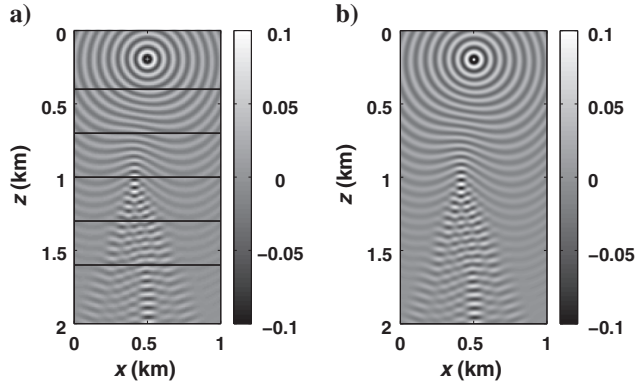

Figure 3. Real part of the wavefield for the sinusoidal model. (a) Obtained by our method (mesh 101×201, solid black lines indicating the locations of secondary sources for each layer) and (b) obtained by the direct Helmholtz solver (mesh 801×1601 and $\omega = 32\pi$). The primary source point is 0.5 and 0.2 km.

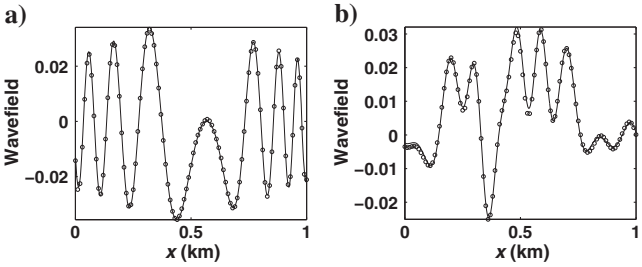

Figure 4. Real part of the wavefield for the sinusoidal model. Comparisons between the solutions obtained by our method and the direct Helmholtz solver at (a) $z = 0.55$ and (b) $z = 1.75$ km, respectively. Solid lines represent solutions by the direct Helmholtz solver, and circles represent solutions by our method ($p = 9$ and $\omega = 32\pi$). The primary source point is 0.5 and 0.2 km.

In stage 2, direct evaluation of the HK-integral induced matrix-vector products is computationally expensive. To accelerate the evaluation, we adapt a multilevel matrix decomposition-based butterfly algorithm originated in Michielssen and Boag (1996) and further developed in O'Neil (2007), Candés et al. (2009), Hu et al. (2013), and Luo et al. (2014a). Following Luo et al. (2014a), given frequency ω, four to six points are specified per wavelength, so that the wavefield is sampled with n mesh points along each spatial direction. For each layer, the complexity of the butterfly algorithm is $O(n^{d-1}(n/L)\log(n^{d-1}(n/L))) = O((N/L)\log N)$, where $N = O(n^d)$, and the prefactor is independent of frequency ω; the complexity of Chebyshev sums and interpolation with respect to secondary sources is $O(N/L)$, where the prefactor depends on the number of spectral coefficients in the truncated Chebyshev expansion. The number of spectral coefficients is considered to be much smaller than $O(n)$. Therefore, the total complexity of constructing the wavefield in the whole domain is $O(N \log N)$ (see Luo et al. [2014a] for more implementation details of the fast butterfly algorithm used here).

Once the data tables are precomputed, the fast Huygens' sweeping method can be used to construct the global wavefield with $O(N \log N)$ complexity for a given primary source and for an arbitrary given frequency. Moreover, the data tables can be reused for many different primary sources. For different primary sources, only the tables with respect to the primary sources inside the first layer are recomputed. The tables of the other layers are reused. Therefore, we refer to stage 1 as "offline" and stage 2 as "online." These unique merits are much desired in many applications, such as seismic imaging and inversion.

NUMERICAL EXAMPLES

We present several numerical experiments to demonstrate our new method. We denote the coarse mesh in stage 1 as GO mesh. We choose $P = 3$ in the high-order factorization for computing τ and B. The mesh for sampling wavefields is chosen such that a fixed number of points (4–6 points) per wavelength are used to resolve wave oscillations. We compare our numerical solutions with those obtained by a direct solver on a much finer mesh. For the direct

Table 1. Sinusoidal model. Numerical accuracy and comparisons on CPU time (s) between the butterfly algorithm-based HK summation (denoted as T_M) and the direct HK summation (denoted as T_D) in the second layer. Here, $p = 9$ Chebyshev nodes are used in each dimension. The source point is 0.5 and 0.2 km. NPW denotes the number of points per wavelength.

Mesh	201×61	401×121	801×241	1601×481	3201×961	6401×1921
$\omega/2\pi$	32	64	128	256	512	1024
NPW	5	5	5	5	5	5
T_D (s)	0.28	1.48	13.12	100.84	810.60	6503.15
			$p = 9$			
L_2 (abs)	1.43E − 5	6.03E − 6	4.06E − 6	4.03E − 6	2.65E − 6	2.37E − 6
L_2 (rel)	1.34E − 3	7.98E − 4	7.62E − 4	1.07E − 3	9.99E − 4	1.26E − 3
T_M (s)	0.61	1.55	4.69	18.30	66.43	299.67
T_M/T_D	0.46	0.95	2.80	5.51	12.20	21.70

finite-difference Helmholtz solver, we use a nine-point stencil (Jo et al., 1996) instead of the usual five-point stencil to reduce dispersion errors and obtain more reliable wavefields; perfectly matched layer absorbing boundary conditions are also imposed (Berenger, 1994). The resulting sparse linear system is solved by the sparse lower-upper triangular (LU) solver in the MATLAB platform.

Example 1: 2D sinusoidal velocity model

In this example, the velocity is chosen as

$$v = 1 + 0.2\,\sin(3\pi(x + 0.05))\,\sin(0.5\pi z)\,(\mathrm{km/s}), \quad (22)$$

on the domain 0.1×0.2 km. In stage 1, the GO coarse mesh is 101×201, and the asymptotic ingredients are compressed with the ratio of 50:1. In stage 2, the separation distance d_f between the sources and receivers is fixed as 0.1 km.

Figure 3 shows the contour plots of the numerical solutions obtained by our approach and the direct Helmholtz solver mentioned above with $\omega = 32\pi$. Our approach uses approximately five points per wavelength, whereas the direct solver uses approximately 40 points per wavelength. Figure 4 shows comparisons between the solutions. Table 1 shows the efficiency and stability of our method and comparisons between the butterfly algorithm and direct summation.

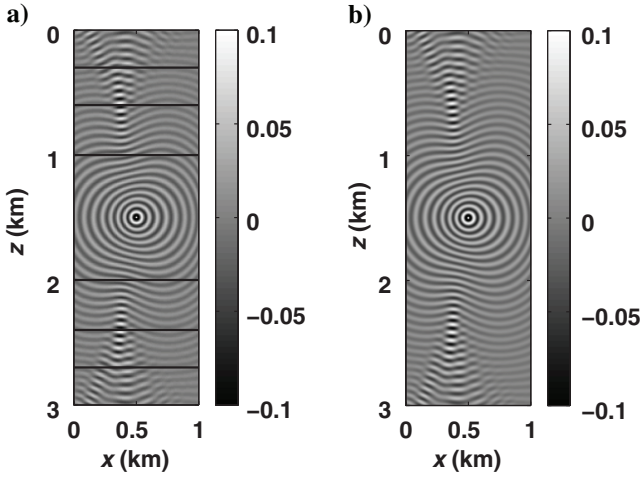

Figure 5. Real part of the wavefield for the sinusoidal model. (a) Obtained by our method (mesh 101×301 and solid black lines indicating the locations of secondary sources for each layer) and (b) obtained by the direct Helmholtz solver (mesh 801×2401 and $\omega = 32\pi$). The primary source point is 0.5 and 1.5 km.

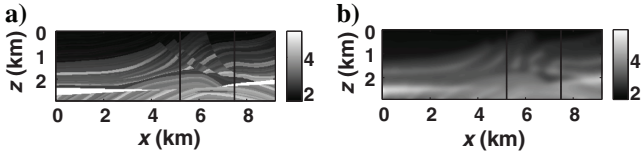

Figure 6. Marmousi model. (a) The original Marmousi velocity field and (b) the smoothed-velocity field. The region between the two black lines is the sampled window from receivers 218 to 313.

Figure 5 shows numerical solutions by our method and the direct solver with a different setup, where the domain is 0.1×0.3 km and the source is at 0.5 and 1.5 km.

Example 2: Synthetic Marmousi velocity model

In this example, we construct wavefields for the Marmousi model. The original model is sampled on a 0.024×0.024 km grid, consisting of 384 samples in the x-direction and 122 samples in the z-direction; therefore, the domain is $[0, 9.192] \times [0, 2.904]$ km. Because we need high-order derivatives of the velocity in high-order approximations, the velocity is smoothed by solving the following least-squares regularization problem:

$$\min_{v(\mathbf{r})} \{|v(\mathbf{r}) - v^m(\mathbf{r})|^2 + \alpha|\nabla_{\mathbf{r}} v(\mathbf{r})|^2 + \beta|\nabla^2_{\mathbf{r}} v(\mathbf{r})|^2\}, \quad (23)$$

where v^m is the original Marmousi model α and β are the smoothness parameters. We choose $\alpha = \beta = 10^{-4}$. Figure 6 shows the Marmousi models. We first test a case with smoothed velocity. The velocity field is a sampled window from receivers 218 to 313 (96 receivers in total) in the smoothed-Marmousi model.

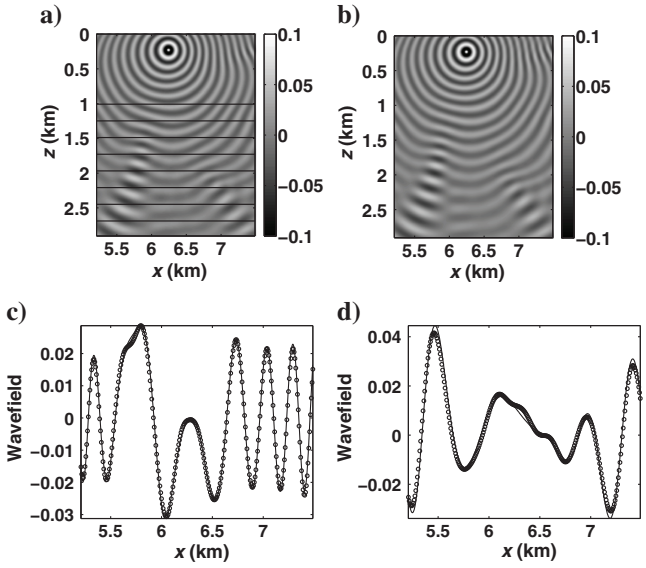

Figure 7. Smoothed-Marmousi model with velocity in Figure 6. Real part of the wavefield (a) obtained by our method, (b) obtained by the direct Helmholtz solver. Solid lines show the positions of the secondary sources, and panels (c and d) are comparisons of the solutions at $z = 1.472$ and 2.592 km, respectively, where circles represent the solution by our method and solid lines represent the solution by the direct Helmholtz solver.

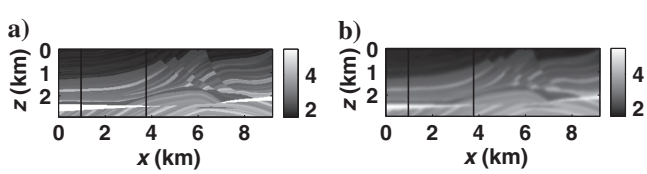

Figure 8. Marmousi model with (a) the original Marmousi velocity field and (b) a slightly smoothed velocity field. The region between the two black lines is the sampled window from receivers 41 to 158.

The windowed domain is $[5.208, 7.488] \times [0, 2.904]$ km. In stage 1, the GO coarse mesh is 96×122 and the asymptotic ingredients are compressed with ratio 25:1. In stage 2, the separation distance d_f between the sources and receivers is fixed at 0.192 km.

We apply our new algorithm to the smoothed-Marmousi velocity model as in Figure 6b. This synthetic geologic structure creates many strong and localized velocity heterogeneities. Figure 7 shows the wavefields with the primary source point given as 5.380 and 0.24 km and $\omega = 32\pi$ by two different methods, where the fast Huygens' sweeping method uses a mesh of 286×364 points, and the direct Helmholtz solver uses a mesh of 1711×2179 points. To apply the direct Helmholtz solver on the fine mesh, the velocity field on the original coarse mesh is interpolated onto the finer mesh first with spline interpolations.

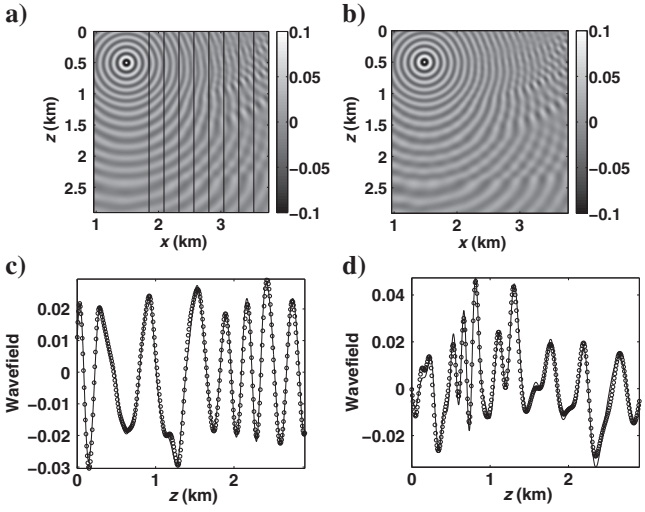

Figure 9. Smoothed-Marmousi model with velocity in Figure 8. Real part of the wavefield (a) obtained by our method and (b) obtained by the direct Helmholtz solver. Solid lines show the positions of the secondary sources, and panels (c and d) are comparisons of the solutions at $x = 2.640$ and 3.360 km, respectively, where circles represent the solution by our method and solid lines represent the solution by the direct Helmholtz solver.

Next, we choose a sampled window from receivers 41 to 158 of the Marmousi model, where the velocity is only slightly smoothed (see Figure 8). The windowed domain is $[0, 2.904] \times [0.96, 3.768]$ km. In stage 1, the GO coarse mesh is 118×122, and the data compression ratio for asymptotic ingredients is 25:1. In stage 2, the separation distance d_f between the sources and receivers is fixed at 0.192 km.

Figure 9 shows the wavefields with the primary source point given as 1.488 and 0.48 km and $\omega = 32\pi$ by the two methods, where the fast Huygens' sweeping method uses a mesh of 352×364 points, and the direct Helmholtz solver uses a mesh of 2107×2179 points. To apply the direct Helmholtz solver on the fine mesh, the velocity field on the original coarse mesh is interpolated onto the finer mesh first with spline interpolations.

Example 3: 3D Vinje et al. (1996) velocity model

In the example, the velocity is chosen as

$$v = 3.0 - 1.75e^{(-((x-1)^2+(y-1)^2+(z-1)^2)/0.64)} \text{ (km/s)}, \quad (24)$$

on the domain $0.2 \times 0.2 \times 0.2$ km. In stage 1, the GO coarse mesh is $51 \times 51 \times 51$ and the data compression ratio for asymptotic ingredients is 32:1. In stage 2, the separation distance d_f between the sources and receivers is fixed at 0.3 km.

We partition the 3D domain into two layers at the plane $z = 1.2$ km. When $\omega = 32\pi$, there are roughly 26 waves propagating in each direction. If a direct solver is used to compute the wavefield, then the number of unknowns is roughly 17 million if 10 points per wavelength are used to capture each wave, resulting in a huge linear system to deal with, not to mention the fact of whether 10 points per wavelength will be sufficient. To use our fast Huygens' sweeping method, we choose approximately four points per wavelength.

Figure 10 shows the results for different primary sources. The tables corresponding to the primary source in the first layer need to be recomputed for different primary sources. Tables with respect to those secondary sources do not need to be recomputed. Table 2 shows the running times of our method for different ω's.

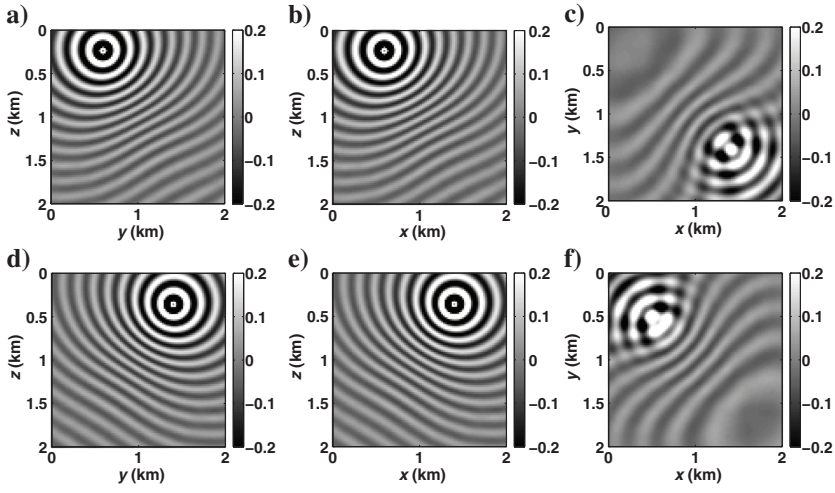

Figure 10. The Vinje model. Wavefields are constructed by our method on a mesh $101 \times 101 \times 101$ with $\omega = 32\pi$. In panels (a-c), the primary point source is 0.6, 0.6, and 0.24 km, and in panels (d-f), the primary source is 1.4, 1.4, and 0.36 km. Panels (a-c) show the real part of the wavefields at $x = 0.6$, $y = 0.6$, and $z = 1.8$ km, respectively, and panels (d- f) show the real part of the wavefields at $x = 1.4$, $y = 1.4$, and $z = 1.8$ km, respectively.

CONCLUSION

We have developed the fast Huygens' sweeping method for evaluating the HK integral, so that locally valid first-arrival Green's functions can be integrated into a globally valid multiarrival Green's function. The needed ingredients for constructing first-arrival Green's functions, such as first-arrival traveltimes and amplitudes, were computed by using a set of newly developed tools, including the factorization approach, the Babich's formulation, power-series-based

Table 2. Vinje model. CPU time (s) for the butterfly algorithm-based HK summation. Here, $p = 7, 9$, and 11 Chebyshev nodes are used in each dimension. The source point is 1.0, 1.0, and 0.2 km. NPW denotes the number of points per wavelength.

Mesh	$101 \times 101 \times 101$	$201 \times 201 \times 201$
$\omega/2\pi$	16	32
NPW	4	4
T_M (s) ($p = 7$)	194.36	1404.61
T_M (s) ($p = 9$)	328.72	2555.59
T_M (s) ($p = 11$)	625.60	4843.46

high-order approximations, and high-order LxF-WENO methods. The HK integrals were evaluated by adapting a fast butterfly algorithm, so that the fast Huygens' sweeping method has computational complexity $O(N \log N)$, where N is the total number of mesh points, and the proportionality constant depends on the desired accuracy as well as is independent of frequency. Numerical examples demonstrated the performance, efficiency, and accuracy of the proposed method.

ACKNOWLEDGMENTS

The authors would like to thank assistant editor J. Shragge, associate editor S. Gray, and the reviewers for constructive comments that helped improve this work significantly. J. Qian is supported by National Science Foundation (NSF)-1222368, and S. Luo is supported by NSF DMS-1418908.

APPENDIX A

COMPRESSION WITH CHEBYSHEV EXPANSION

We illustrate the compression process for a 3D traveltime table. The same can be done for amplitude and takeoff angle tables and for 2D tables (Boyd, 2001; Alkhalifah, 2011). Without a loss of generality, we assume that the traveltime $\tau(\mathbf{r};\mathbf{r}_0)$ is defined on $[-1,1]^3$ for a given source point $\mathbf{r}_0$. The τ can be expanded in terms of Chebyshev polynomials of the first kind (Boyd, 2001):

$$\tau(\mathbf{r};\mathbf{r}_0) = \tau(x,y,z;\mathbf{r}_0) = \sum_{m=0}^{\infty}\sum_{n=0}^{\infty}\sum_{k=0}^{\infty} C_{mnk}(\mathbf{r}_0)T_m(x)T_n(y)T_k(z), \quad \text{(A-1)}$$

where $T_l(\cdot)$ is the Chebyshev polynomial of the first kind and of order l: $T_l(\cdot) = \cos(l\cos^{-1}(\cdot))$ and $\{C_{mnk}(\mathbf{r}_0)\}$ are spectral coefficients. To determine $\{C_{mnk}(\mathbf{r}_0)\}$, we use the computed traveltime on the coarse mesh in stage 1. The $\{C_{mnk}(\mathbf{r}_0)\}$ are then computed with the fast Fourier cosine transform (Boyd, 2001; Alkhalifah, 2011). In numerical applications, for a given accuracy it is enough to keep only the first few coefficients among $\{C_{mnk}(\mathbf{r}_0)\}$:

$$\tau(\mathbf{r};\mathbf{r}_0) = \tau(x,y,z;\mathbf{r}_0) \approx \sum_{m=0}^{C_X-1}\sum_{n=0}^{C_Y-1}\sum_{k=0}^{C_Z-1} C_{mnk}(\mathbf{r}_0)T_m(x)T_n(y)T_k(z), \quad \text{(A-2)}$$

with C_X, C_Y, and C_Z being the given numbers. Instead of saving τ on the coarse mesh, the set of significant coefficients,

$$\tilde{C} = \{C_{mnk}(\mathbf{r}_0): 0 \le m \le C_X - 1, \; 0 \le n \le C_Y - 1, \quad 0 \le k \le C_Z - 1\}, \quad \text{(A-3)}$$

will be saved for later use. In practice, it is possible to reconstruct τ with high accuracy even with a relatively high compression ratio defined as (the size of the coarse mesh)$/(C_X C_Y C_Z)$.

With $\tilde{C}$, the traveltime on any specified computational mesh can be computed by evaluating formula A-2 on that mesh as product of low-rank matrices, which is detailed below using MATLAB notation:

- In 3D, τ on a mesh of size $M \times N \times K$ spanned by $\mathbf{X} = [-1:h_x:1]$, $\mathbf{Y} = [-1:h_y:-1]$, and $\mathbf{Z} = [-1:h_z:1]$ is reconstructed by

$$\tau = \text{permute}(\text{permute}(\mathbf{T_X}'\tilde{C}\mathbf{T_Z}, [1 \quad 3 \quad 2])\mathbf{T_Y}, [1 \quad 3 \quad 2]), \quad \text{(A-4)}$$

  where $\mathbf{T_X}$, $\mathbf{T_Y}$, and $\mathbf{T_Z}$ are of size $C_X \times M$, $C_Y \times N$, and $C_Z \times K$, respectively, and

$$\mathbf{T_X}(l,:) = T_{l-1}(\mathbf{X}), \quad \mathbf{T_Y}(l,:) = T_{l-1}(\mathbf{Y}), \quad \text{and} \quad \mathbf{T_Z}(l,:) = T_{l-1}(\mathbf{Z}). \quad \text{(A-5)}$$

- In 2D, τ on a 2D mesh of size $M \times K$ spanned by $\mathbf{X} = [-1:h_x:1]$ and $\mathbf{Z} = [-1:h_z:1]$ is reconstructed as

$$\tau = \mathbf{T_X}'\tilde{C}\mathbf{T_Z}, \quad \text{(A-6)}$$

  where $\tilde{C}$ is of size $C_X \times C_Z$.

REFERENCES

Albertin, U., D. Yingst, P. Kitchenside, and V. Tcheverda, 2004, True-amplitude beam migration: 74th Annual International Meeting, SEG, Expanded Abstracts, 949–952.

Alkhalifah, T., 2011, Efficient traveltime compression for 3D prestack Kirchhoff migration: Geophysical Prospecting, **59**, 1–9, doi: 10.1111/j.1365-2478.2010.00886.x.

Alkhalifah, T., and S. Fomel, 2010, An eikonal-based formulation for traveltime perturbation with respect to the source location: Geophysics, **75**, no. 6, T175–T183, doi: 10.1190/1.3490390.

Babich, V. M., 1965, The short wave asymptotic form of the solution for the problem of a point source in an inhomogeneous medium: USSR Computational Mathematics and Mathematical Physics, **5**, 247–251, doi: 10.1016/0041-5553(65)90021-2.

Babuskar, I. M., and S. A. Sauter, 2000, Is the pollution effect of the FEM avoidable for the Helmholtz equation considering high wavenumbers?: SIAM Review, **42**, 451–484, doi: 10.1137/S0036142994269186.

Baker, B., and E. T. Copson, 1987, The mathematical theory of Huygens' principle: Ams Chelsea Publishing.

Bao, G., J. Lai, and J. Qian, 2014, Fast multiscale Gaussian beam methods for wave equations in bounded domains: Journal of Computational Physics, **261**, 36–64, doi: 10.1016/j.jcp.2013.12.034.

Benamou, J. D., S. Luo, and H.-K. Zhao, 2010, A compact upwind second order scheme for the eikonal equation: Journal of Computational Mathematics, **28**, 489–516.

Berenger, J.-P., 1994, A perfectly matched layer for the absorption of electromagnetic waves: Journal of Computational Physics, **114**, 185–200, doi: 10.1006/jcph.1994.1159.

Berryhill, J. R., 1979, Wave-equation datuming: Geophysics, **44**, 1329–1344, doi: 10.1190/1.1441010.

Bevc, D., 1997, Imaging complex structures with semirecursive Kirchhoff migration: Geophysics, **62**, 577–588, doi: 10.1190/1.1444167.

Boyd, J. P., 2001, Chebyshev and Fourier spectral methods, 2nd ed.: Dover.
Burridge, R., 1962, The reflexion of high-frequency sound in a liquid sphere: Proceedings of the Royal Society of London, Series A, **270**, 144–154, doi: 10.1098/rspa.1962.0208.
Candés, E., L. Demanet, and L. Ying, 2009, A fast butterfly algorithm for the computation of Fourier integral operators: Multiscale Modeling and Simulation, **7**, 1727–1750, doi: 10.1137/080734339.
Červený, V., I. A. Molotkov, and I. Psencik, 1977, Ray method in seismology: Univerzita Karlova Press.
Červený, V., M. Popov, and I. Psencik, 1982, Computation of wave fields in inhomogeneous media: Gaussian beam approach: Geophysical Journal of the Royal Astronomical Society, **70**, 109–128, doi: 10.1111/j.1365-246X.1982.tb06394.x.
Chapman, C. H., 1985, Ray theory and its extensions: WKBJ and Maslov seismogram: Journal of Geophysics, **58**, 27–43.
Fomel, S., S. Luo, and H.-K. Zhao, 2009, Fast sweeping method for the factored eikonal equation: Journal of Computational Physics, **228**, 6440–6455, doi: 10.1016/j.jcp.2009.05.029.
Franklin, J., and J. M. Harris, 2001, A high-order fast marching scheme for the linearized eikonal equation: Journal of Computational Acoustics, **9**, 1095–1109, doi: 10.1142/S0218396X01000784.
Geoltrain, S., and J. Brac, 1993, Can we image complex structures with first-arrival traveltime: Geophysics, **58**, 564–575, doi: 10.1190/1.1443439.
Gray, S., 2005, Gaussian beam migration of common shot records: Geophysics, **70**, no. 4, S71–S77, doi: 10.1190/1.1988186.
Gray, S., and W. May, 1994, Kirchhoff migration using eikonal equation traveltimes: Geophysics, **59**, 810–817, doi: 10.1190/1.1443639.
Hill, N., 1990, Gaussian beam migration: Geophysics, **55**, 1416–1428, doi: 10.1190/1.1442788.
Hole, J., and B. C. Zelt, 1995, 3-D finite-difference reflection traveltimes: Geophysical Journal International, **121**, 427–434, doi: 10.1111/j.1365-246X.1995.tb05723.x.
Hu, C., and P. Stoffa, 2009, Slowness-driven Gaussian-beam prestack depth migration for low-fold seismic data: Geophysics, **74**, no. 6, WCA35–WCA45, doi: 10.1190/1.3250268.
Hu, J., S. Fomel, L. Demanet, and L. Ying, 2013, A fast butterfly algorithm for generalized Radon transforms: Geophysics, **78**, no. 4, U41–U51, doi: 10.1190/geo2012-0240.1.
Jo, C.-H., C. Shin, and J. H. Suh, 1996, An optimal 9-point, finite-difference, frequency-space, 2-D scalar wave extrapolator: Geophysics, **61**, 529–537, doi: 10.1190/1.1443979.
Kao, C. Y., S. Osher, and J. Qian, 2004, Lax-Friedrichs sweeping schemes for static Hamilton-Jacobi equations: Journal of Computational Physics, **196**, 367–391, doi: 10.1016/j.jcp.2003.11.007.
Kim, S., and R. Cook, 1999, 3-D traveltime computation using second-order ENO scheme: Geophysics, **64**, 1867–1876, doi: 10.1190/1.1444693.
Leung, S., and J. Qian, 2006, An adjoint state method for three-dimensional transmission traveltime tomography using first-arrivals: Communications in Mathematical Sciences, **4**, 249–266, doi: 10.4310/CMS.2006.v4.n1.a10.
Leung, S., and J. Qian, 2010, The backward phase flow and FBI-transform-based Eulerian Gaussian beams for the Schrödinger equation: Journal of Computational Physics, **229**, 8888–8917, doi: 10.1016/j.jcp.2010.08.015.
Leung, S., J. Qian, and R. Burridge, 2007, Eulerian Gaussian beams for high-frequency wave propagation: Geophysics, **72**, no. 5, SM61–SM76, doi: 10.1190/1.2752136.
Li, S., and S. Fomel, 2013, Kirchhoff migration using eikonal-based computation of traveltime source derivative: Geophysics, **78**, no. 4, S211–S219, doi: 10.1190/geo2012-0375.1.
Luo, S., and J. Qian, 2011, Factored singularities and high-order Lax-Friedrichs sweeping schemes for point-source traveltimes and amplitudes: Journal of Computational Physics, **230**, 4742–4755, doi: 10.1016/j.jcp.2011.02.043.
Luo, S., and J. Qian, 2012, Fast sweeping methods for factored anisotropic eikonal equations: Multiplicative and additive factors: Journal of Scientific Computing, **52**, 360–382, doi: 10.1007/s10915-011-9550-y.
Luo, S., J. Qian, and R. Burridge, 2014a, Fast Huygens sweeping methods for Helmholtz equations in inhomogeneous media in the high frequency regime: Journal of Computational Physics, **270**, 378–401, doi: 10.1016/j.jcp.2014.03.066.
Luo, S., J. Qian, and R. Burridge, 2014b, High-order factorization based high-order hybrid fast sweeping methods for pointsource eikonal equations: SIAM Journal on Numerical Analysis, **52**, 23–44, doi: 10.1137/120901696.
Luo, S., J. Qian, and H.-K. Zhao, 2012, Higher-order schemes for 3-D traveltimes and amplitudes: Geophysics, **77**, no. 2, T47–T56, doi: 10.1190/geo2010-0363.1.
Michielssen, E., and A. Boag, 1996, A multilevel matrix decomposition algorithm for analyzing scattering from large structures: IEEE Transactions on Antennas and Propagation, **44**, 1086–1093, doi: 10.1109/8.511816.
Milnor, J., 1963, Morse theory: Princeton University Press.
Nichols, D., 1994, Imaging complex structures using band limited Green's functions: Ph.D. thesis, Stanford University.
O'Neil, M., 2007, A new class of analysis-based fast transforms: Doctoral dissertation, Yale University.
Operto, S., S. Xu, and G. Lambare, 2000, Can we image quantitatively complex models with rays?: Geophysics, **65**, 1223–1238, doi: 10.1190/1.1444814.
Pica, A., 1997, Fast and accurate finite-difference solutions of the 3D eikonal equation parametrized in celerity: 67th Annual International Meeting, SEG, 1774–1777.
Popov, M. M., 1982, A new method of computation of wave fields using Gaussian beams: Wave Motion, **4**, 85–97, doi: 10.1016/0165-2125(82)90016-6.
Qian, J., and W. W. Symes, 2002a, An adaptive finite-difference method for traveltimes and amplitudes: Geophysics, **67**, 167–176, doi: 10.1190/1.1451472.
Qian, J., and W. W. Symes, 2002b, Finite-difference quasi-P traveltimes for anisotropic media: Geophysics, **67**, 147–155, doi: 10.1190/1.1451438.
Qian, J., and L. Ying, 2010a, Fast Gaussian wavepacket transforms and Gaussian beams for the Schrödinger equation: Journal of Computational Physics, **229**, 7848–7873, doi: 10.1016/j.jcp.2010.06.043.
Qian, J., and L. Ying, 2010b, Fast multiscale Gaussian wavepacket transforms and multiscale Gaussian beams for the wave equation: Multiscale Modeling and Simulation, **8**, 1803–1837, doi: 10.1137/100787313.
Qian, J., Y.-T. Zhang, and H.-K. Zhao, 2007a, A fast sweeping method for static convex Hamilton-Jacobi equations: Journal of Scientific Computing, **31(1/2)**, 237–271, doi: 10.1007/s10915-006-9124-6.
Qian, J., Y.-T. Zhang, and H.-K. Zhao, 2007b, Fast sweeping methods for eikonal equations on triangulated meshes: SIAM Journal on Numerical Analysis, **45**, 83–107, doi: 10.1137/050627083.
Qin, F., Y. Luo, K. B. Olsen, W. Cai, and G. T. Schuster, 1992, Finite difference solution of the eikonal equation along expanding wavefronts: Geophysics, **57**, 478–487, doi: 10.1190/1.1443263.
Ralston, J., 1983, Gaussian beams and the propagation of singularities, *in* W. Littman, ed., Studies in partial differential equations: Mathematical Association of America Studies in Mathematics, 206–248.
Schneider, W. A. J., 1995, Robust and efficient upwind finite-difference traveltime calculations in three dimensions: Geophysics, **60**, 1108–1117, doi: 10.1190/1.1443839.
Schneider, W. A. J., K. Ranzinger, A. Balch, and C. Kruse, 1992, A dynamic programming approach to first arrival traveltime computation in media with arbitrarily distributed velocities: Geophysics, **57**, 39–50, doi: 10.1190/1.1443187.
Serna, S., and J. Qian, 2010, A stopping criterion for higher-order sweeping schemes for static Hamilton-Jacobi equations: Journal of Computational Mathematics, **28**, 552–568, doi: 10.4208/jcm.1003-m0016.
Sethian, J. A., and A. M. Popovici, 1999, 3-D traveltime computation using the fast marching method: Geophysics, **64**, 516–523, doi: 10.1190/1.1444558.
Symes, W. W., and J. Qian, 2003, A slowness matching Eulerian method for multivalued solutions of eikonal equations: Journal of Scientific Computing, **19**, 501–526, doi: 10.1023/A:1025380731197.
Tanushev, N., J. Qian, and J. Ralston, 2007, Mountain waves and Gaussian beams: Multiscale Modeling and Simulation, **6**, 688–709, doi: 10.1137/060673667.
Tsai, Y.-H., L.-T. Cheng, S. Osher, and H.-K. Zhao, 2003, Fast sweeping algorithms for a class of Hamilton-Jacobi equations: SIAM Journal on Numerical Analysis, **41**, 673–694, doi: 10.1137/S0036142901396533.
Van Trier, J., and W. W. Symes, 1991, Upwind finite-difference calculation of traveltimes: Geophysics, **56**, 812–821, doi: 10.1190/1.1443099.
Vidale, J. E., 1990, Finite-difference calculation of traveltimes in three dimensions: Geophysics, **55**, 521–526, doi: 10.1190/1.1442863.
Vinje, V., E. Iversen, K. Astebol, and H. Gjoystdal, 1996, Estimation of multivalued arrivals in 3D models using wavefront construction: Geophysical Prospecting, **44**, 819–842, doi: 10.1111/j.1365-2478.1996.tb00175.x.
Zhang, L., J. W. Rector, and G. M. Hoversten, 2005, Eikonal solver in the celerity domain: Geophysical Journal International, **162**, 1–8, doi: 10.1111/j.1365-246X.2005.02626.x.
Zhang, Y. T., H. K. Zhao, and J. Qian, 2006, High order fast sweeping methods for static Hamilton-Jacobi equations: Journal of Scientific Computing, **29**, 25–56, doi: 10.1007/s10915-005-9014-3.
Zhao, H.-K., 2005, A fast sweeping method for eikonal equations: Mathematics of Computation, **74**, 603–628., doi: 10.1090/S0025-5718-04-01678-3.